

ARTICLE

DOI: 10.1038/s42004-018-0086-z

OPEN

Cobalt doping of tin disulfide/reduced graphene oxide nanocomposites for enhanced pseudocapacitive sodium-ion storage

Hao Jia¹, Chen Chen², Olabode Oladele³, Yongan Tang³, Guoqing Li⁴, Xiangwu Zhang¹ & Fei Yan ²

Rechargeable sodium-ion batteries are receiving intense interest as a promising alternative to lithium-ion batteries, however, the absence of high-performance anode materials limits their further commercialization. Here we prepare cobalt-doped tin disulfide/reduced graphene oxide nanocomposites via a microwave-assisted hydrothermal approach. These nanocomposites maintain a capacity of 636.2 mAh g⁻¹ after 120 cycles under a current density of 50 mA g⁻¹, and display a capacity of 328.3 mA h g⁻¹ after 1500 cycles under a current density of 2 A g⁻¹. The quantitative capacitive analysis demonstrates that the electrochemical performance of the nanocomposite originates from the combined effects of cobalt and sulfur doping, resulting in the enhanced pseudocapacitive contribution (52.8 to 89.8% at 1 mV s⁻¹) of tin disulfide. This work provides insight into tuning the structure of layered transition metal dichalcogenides via heteroatom doping to develop high-performance anode materials for sodium-ion batteries.

¹Department of Textile Engineering, Chemistry and Science, North Carolina State University, Raleigh, NC 27695, USA. ²Department of Chemistry and Biochemistry, North Carolina Central University, Durham, NC 27707, USA. ³Department of Mathematics and Physics, North Carolina Central University, Durham, NC 27707, USA. ⁴Department of Materials Science and Engineering, North Carolina State University, Raleigh, NC 27695, USA. These authors contributed equally: Hao Jia and Chen Chen. Correspondence and requests for materials should be addressed to F.Y. (email: fyan@ncsu.edu)

Lithium-ion batteries (LIBs), the most commonly used type of secondary batteries, have achieved great success in the last decades and been widely integrated into various applications such as portable electronics, hybrid electric vehicles (HEVs) and so on^{1,2}. However, the uneven distribution and relatively low abundance of lithium resource make it difficult to meet the rapidly growing needs of these applications. Sodium-ion batteries (SIBs), as a complementary alternative to LIBs for large-scale grid energy storage systems, have been attracting extensive attention owing to the abundance of sodium (Na) and improved operating safety^{3,4}. Currently, one of the major challenges to realize commercialization of SIBs for market application is the lack of suitable anode materials with high capacity, fast, and durable sodium storage.

On the basis of the combined conversion and alloying reaction, the layered metal sulfides such as tin disulfide (SnS_2) and molybdenum disulfide (MoS_2), show great promise for SIB anode application due to their demonstrated superior performance. Among these metal sulfides, SnS_2 has a typical layered structure with large interlamellar spacing ($d = 0.5899 \text{ nm}$), which has drawn tremendous attention because of its high theoretical capacity of 1232 mAh g^{-1} , ease to intercalation with Na^+ and natural abundance. In addition, the relatively weaker Sn–S ionic bonds make SnS_2 kinetically favorable and higher first-cycle efficiency. Despite these advantages, the electrochemical performance of bare SnS_2 is still not satisfactory, which is mainly caused by the sluggish reaction kinetics and severe volume change during the sodiation/desodiation process, leading to the poor rate capability and cycling stability. Generally, in order to overcome these limitations and to achieve an excellent Na storage performance, the metal sulfide anode materials should have the following properties: (1) increased interlayer spacing in the layered structure benefiting Na^+ diffusion and intercalation; (2) better relief of the volume changes during cycling; (3) fast conduction and transportation of electrons through a highly conductive network; (4) inhibition of nanoparticle (such as Na_xSn) aggregation during cycling; and (5) easy synthesis process. On the other hand, two Na-ion storage mechanisms have been revealed in various electrode materials: (i) the diffusion-controlled intercalation/conversion/alloying process and (ii) the surface-induced capacitive

process, which refers to the faradaic charge transfer reactions including surface or near-surface redox reactions and bulk fast ion intercalation. Compared with the diffusion-controlled process, the capacitive charge storage can endow the electrode high capacity under high charge and discharge rate, leading to high power of the electrode. Given these considerations, a promising route to fulfill these requirements is to produce SnS_2 /carbon composite using an ultra-fast and energy-efficient way to nano-manufacture metal chalcogenides, whereby the carbon network provides good conductivity and can buffer the large volume changes induced by charging. Meanwhile, decreasing the active material sizes preferably to the nanometer scale, not only can decrease the deformation and the cracking susceptibility, but also can shorten the diffusion path to maximize the pseudocapacitive contribution. By elaborately adopting heteroatoms inside the SnS_2 structures such as Mo, Fe, Ce, and Co, it can effectively limit the number of layers of nanosheets, enlarge the interlayer spacing and generate rich defects as active sites for sodiation/desodiation^{5–7}.

Here, we report a Co-doped SnS_2 /RGO composite prepared via an ultra-fast microwave-synthesis approach. After the Co doping, the pseudocapacitance of SnS_2 /RGO is significantly enhanced, as inferred from the increased capacitive contribution during cycling. Owing to this enhanced pseudocapacitive effect, limited few-layer structure, enlarged interlayer spacing and rich defects, the rationally designed Co-doped SnS_2 /RGO electrode exhibits enhanced reversible capacity, rate capability, and cycling stability as SIB anode, demonstrating that heteroatom doping is a feasible and general strategy for structural modification on metal chalcogenides to improve their electrochemical performance.

Results

Structural characterization. Figure 1 illustrates the overall fabrication procedure of the flexible RGO-supported Co-doped SnS_2 through a rapid one-step in situ microwave route. Briefly, when SnCl_4 and CoCl_2 was dissolved in a graphene oxide solution, Sn^{4+} and Co^{2+} were attracted over the GO surface because of the strong electrostatic interactions with surface functionalities. Then under microwave irradiation, L-cysteine would decompose and release hydrogen sulfide to sulfurize the Sn^{4+} and Co^{2+} into Co-

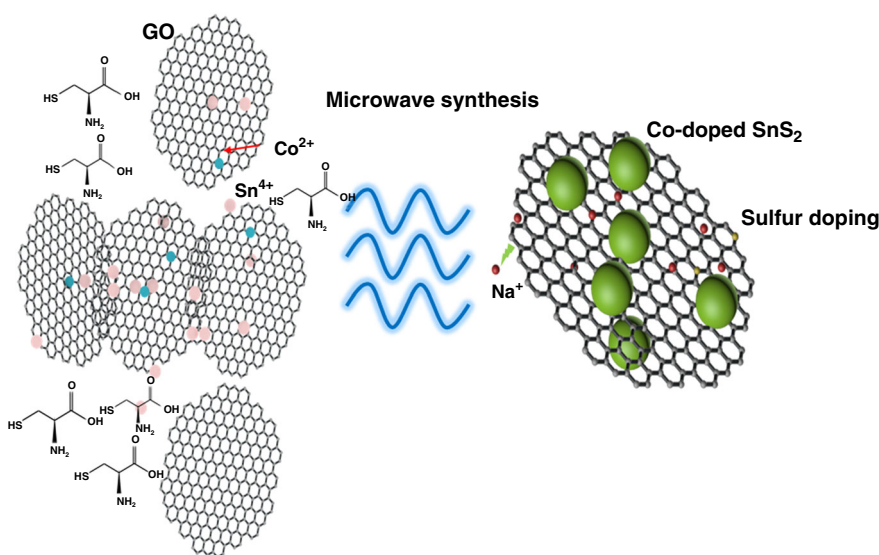


Fig. 1 Synthesis scheme. Co-doped SnS_2 /RGO nanocomposites are prepared via a one-step microwave-assisted hydrothermal approach. Under microwave irradiation, L-cysteine decomposes and releases hydrogen sulfide to sulfurize the Sn^{4+} and Co^{2+} , which are attracted to the GO surface due to the strong electrostatic interactions. Excess sulfur is being incorporated into RGO layers, resulting in a sulfur doping effect

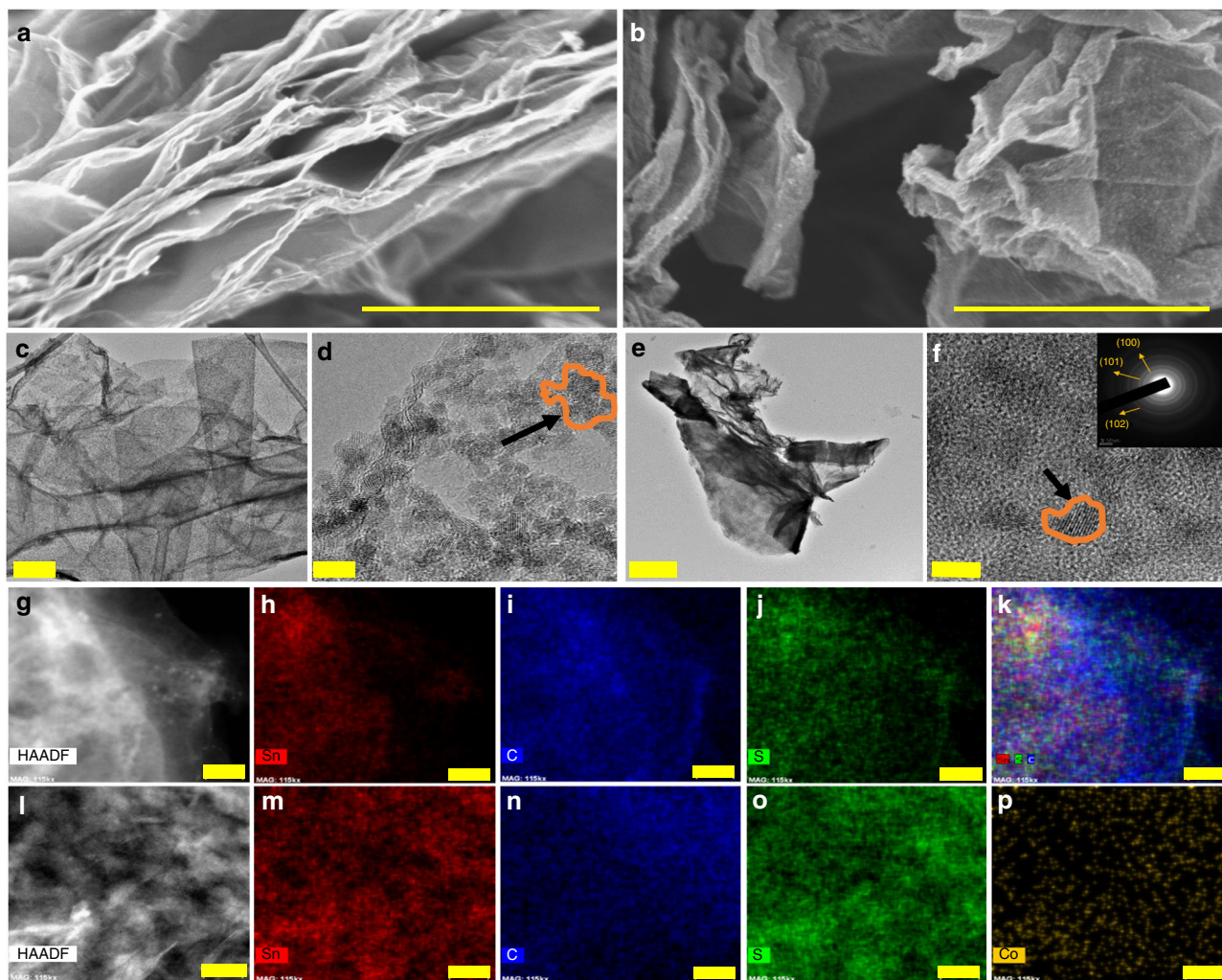


Fig. 2 Direct evidence of cobalt doping of SnS_2/RGO . **a** SEM image of SnS_2/RGO , scale bar: $1\ \mu\text{m}$. **b** SEM image of $\text{Sn}_{0.9}\text{Co}_{0.1}\text{S}_x/\text{RGO}$, scale bar: $1\ \mu\text{m}$. **c** TEM image of SnS_2/RGO , scale bar: $0.5\ \mu\text{m}$. **d** TEM image of SnS_2/RGO , scale bar: $5\ \text{nm}$. **e** TEM image of $\text{Sn}_{0.9}\text{Co}_{0.1}\text{S}_x/\text{RGO}$, scale bar: $0.5\ \mu\text{m}$. **f** TEM image of $\text{Sn}_{0.9}\text{Co}_{0.1}\text{S}_x/\text{RGO}$, scale bar: $5\ \text{nm}$. The inset is selected-area diffraction (SAED) pattern; **g–k** High-angle annular dark-field (HAADF) image and composite RGB element maps of SnS_2/RGO , and **l–p** HAADF image and composite RGB element maps of $\text{Sn}_{0.9}\text{Co}_{0.1}\text{S}_x/\text{RGO}$ with corresponding TEM image. The scale bar for **g–p** represents $100\ \text{nm}$. Co, Sn and S elements are homogeneously distributed over the carbon and throughout the $\text{Sn}_{0.9}\text{Co}_{0.1}\text{S}_x/\text{RGO}$, suggesting the successful Co doping in the SnS_2 crystal lattice

doped SnS_2 nanocrystals, anchoring on the RGO layers. Meanwhile, the graphene oxide would be reduced into RGO and some excess sulfur was believed to incorporate into RGO layers, resulting in a sulfur doping effect on the RGO. The decomposition process of L-cysteine could be inferred as the following equation.



The microstructure and morphology of the composites were first observed by SEM and TEM. As shown in Fig. 2a, b, the SnS_2 and Co-doped SnS_2 nanoparticles anchor intimately on the highly crumpling and flexible RGO matrix without obvious aggregation, suggesting that RGO could act as a heterogeneous dispersing agent during the particle formation process. Compared with $\text{SnS}_2/50\text{RGO}$ (Supplementary Fig. 1b), some RGO sheets without sufficient coverage of SnS_2 nanoparticles can be found in the $\text{SnS}_2/75\text{RGO}$ composites (Supplementary Fig. 1a) and therefore, a lower specific capacity will be expected. On the other hand, in the case of $\text{SnS}_2/15\text{RGO}$ and $\text{SnS}_2/25\text{RGO}$ composites, excess

nanoparticle agglomeration is evident on the surface of the RGO matrix, which may cause capacity decay during the charge/discharge process, leading to poor cycling stability. As Fig. 2c–f illustrate, the appearance of highly transparent RGO in the TEM images indicate few-layer structure, which enables a good flexibility and large contact surface area with the electrolyte during cycling. The SnS_2 and $\text{Sn}_{0.9}\text{Co}_{0.1}\text{S}_x$ nanoparticles have an average size around $3\text{--}10\ \text{nm}$. Generally, it is believed that severe aggregation of active nanoparticles may cause large volume changes upon cycling and loss of electrical contact with the RGO matrix, causing a fast capacity decay during cycling. Therefore, homogeneous dispersion of nanoparticles on the RGO is critical to the cycling stability. For some areas of SnS_2/RGO (Fig. 2d), it is found that the SnS_2 nanoparticles cluster into large particles without clear boundaries with each other, on the contrary, the ultrafine $\text{Sn}_{0.9}\text{Co}_{0.1}\text{S}_x$ nanoparticles have a more homogeneous distribution onto the RGO and the small nanoparticle sizes are well maintained. It is believed that the existence of Co^{2+} during the microwave process could strongly disrupt on the growth process of SnS_2 crystals by increasing the energy barrier of nanoparticle formation and preventing its continuous growth,

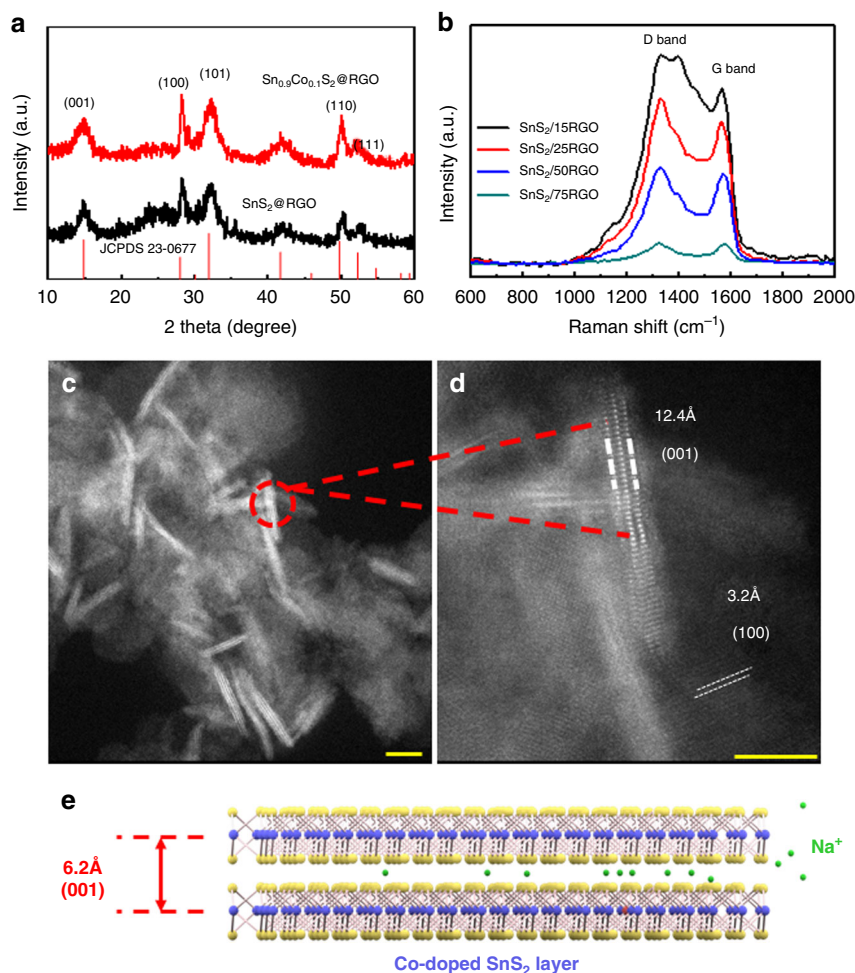


Fig. 3 Structure characterization. **a** XRD patterns of SnS₂/RGO and Sn_{0.9}Co_{0.1}S_x/RGO. **b** Raman spectra of SnS₂/15RGO, SnS₂/25RGO, SnS₂/50RGO and SnS₂/75RGO; **c, d** High-resolution TEM images of Sn_{0.9}Co_{0.1}S_x. The scale bars for **c** and **d** are 10 nm and 5 nm, respectively. **e** Schematic illustrations of (001) and (100) facets of its lamellar structure. Co doping generates an expansion of the interlayer spacing in the SnS₂ crystal lattice, which is consistent with the XRD results

forming small sizes and homogeneous distribution of Sn_{0.9}Co_{0.1}S_x. Moreover, since that the diffusion time of ions (t) is proportional to the square of the diffusion length (L), $t \approx L^2/D$, the small particle sizes of Sn_{0.9}Co_{0.1}S_x can facilitate fast kinetics of Na⁺. The selected-area electron diffraction (SAED) patterns of the Sn_{0.9}Co_{0.1}S_x/RGO shows well-defined diffraction rings, which can be assigned to (100), (101), and (102) crystal planes, respectively, which suggests the well-crystallized Sn_{0.9}Co_{0.1}S_x.

The elemental mapping results (as shown in Fig. 2g–p) unambiguously confirmed the existence of C, Sn, S, and Co elements in the as-prepared SnS₂/RGO and Sn_{0.9}Co_{0.1}S_x/RGO. For SnS₂@RGO, the Sn and S elements are homogeneously distributed over the carbon and Co is also uniformly distributed throughout the Sn_{0.9}Co_{0.1}S_x/RGO, suggesting the successful Co doping in the SnS₂ crystal lattice.

The crystalline structure of the resultant composites was studied by XRD (Fig. 3a). The sharp diffraction peaks can be ascribed to (001), (100), (101), (110), and (111) planes, indicating the hexagonal crystal structure of SnS₂ (JCPDS-23-0677). In addition, there were no peaks corresponding to cobalt sulfide or metal oxides, could be found in the XRD results, suggesting a well incorporation of cobalt ions into the crystal lattice of hexagonal phase SnS₂. As Figure S2 represents, the (001) peak intensity

gradually decreases with decreasing weight ratio of SnS₂/RGO, indicative of the greatly suppressed growth of the (001) crystal plane and a preferential c -axis orientation of SnS₂ plates after integration with GO⁸. It has been reported by others that the heteroatom doping could efficiently restrain the growth of the (001) plane of SnS₂, leading to thinner nanosheets^{5–7}. From the Fig. 3a, it is seen that the (001) peak intensity of Sn_{0.9}Co_{0.1}S_x/RGO is relatively weak, confirming the limited growth of Sn_{0.9}Co_{0.1}S_x along (001) plane. Moreover, after the Co doping, the (100) peak shifted to lower angle (Supplementary Fig. 2b). Therefore, using the Bragg equation, it can be calculated that the (100) lattice spacing (d) of Sn_{0.9}Co_{0.1}S_x was expanded. Further structural characteristics of the RGO matrix were investigated via Raman spectroscopy. As seen in Fig. 3b, the D band (~1336 cm⁻¹) corresponds to disorder and defects in the hexagonal graphitic layers, while the G band (~1574 cm⁻¹) could be ascribed to the first-order scattering of the E_{2g} mode of sp² carbon atoms⁹. The calculated I_D/I_G ratios for different L-Cysteine/GO ratios are 1.19, 1.15, 1.07, and 1.06 for SnS₂/15RGO, SnS₂/25RGO, SnS₂/50RGO, and SnS₂/75RGO, respectively. This correlation suggests that as the relative RGO content decreased, the sulfuration process created more defects on the RGO, resulting in more disorder and low graphitization structures and it has been proved these rich

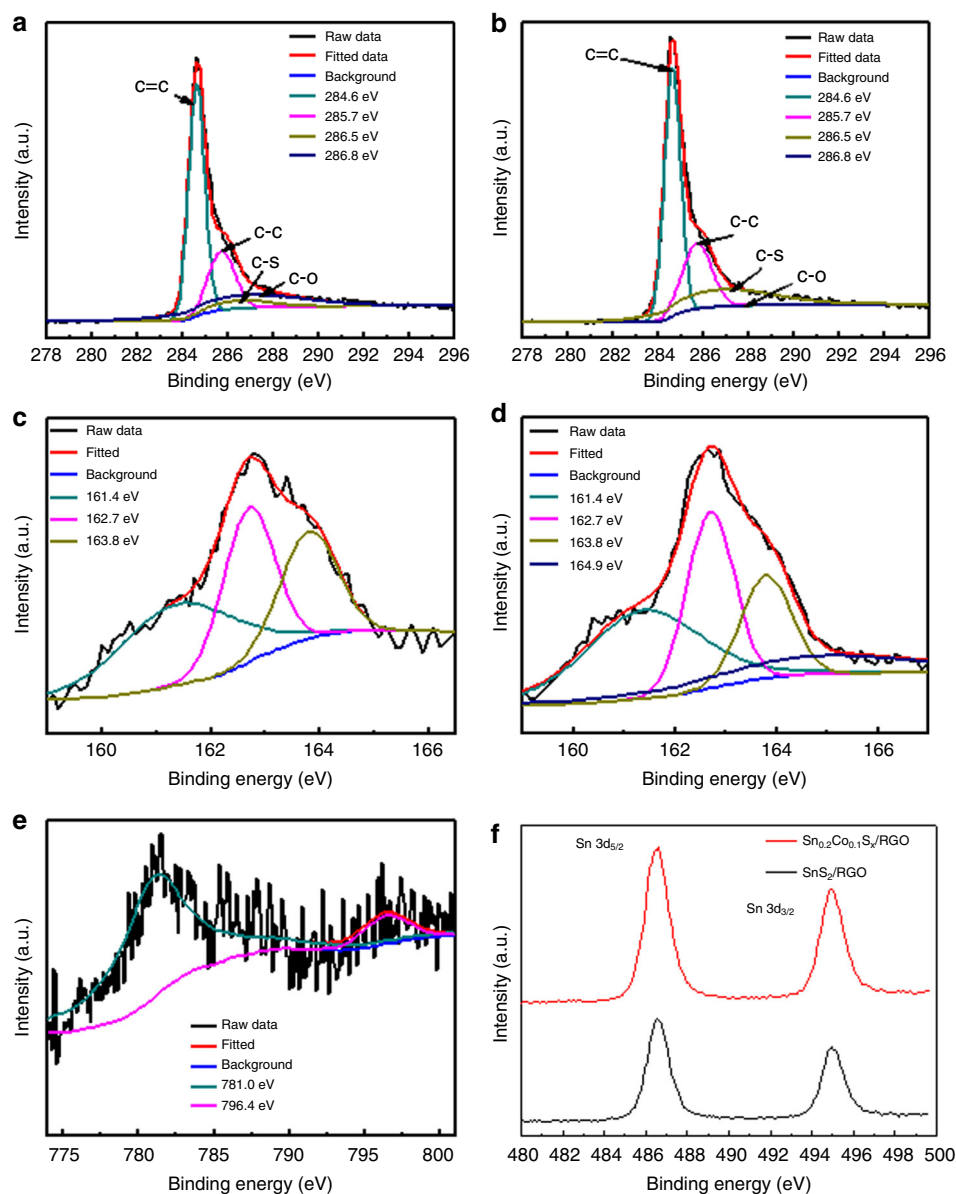


Fig. 4 XPS analysis. High-resolution XPS spectra of **a** C 1s spectra of $\text{Sn}_{0.9}\text{Co}_{0.1}\text{S}_x/\text{RGO}$. **b** C 1s spectra of SnS_2/RGO . **c** S 2p spectra of $\text{Sn}_{0.9}\text{Co}_{0.1}\text{S}_x/\text{RGO}$. **d** S 2p spectra of SnS_2/RGO . **e** Co 2p spectra of $\text{Sn}_{0.9}\text{Co}_{0.1}\text{S}_x/\text{RGO}$. **f** Sn 3d spectra of SnS_2/RGO and $\text{Sn}_{0.9}\text{Co}_{0.1}\text{S}_x/\text{RGO}$. Several O atoms in GO have been successfully substituted by S atoms, leading to S doping effect on the RGO

defects on the RGO play a key role in Na^+ mobility and transportation enhancement, giving rise to improved electrochemical performance^{1,10,11}.

A detailed plausible mechanism of the growth of SnS_2 is also proposed: during the microwave treatment, due to the interaction between the functional group of GO surface and Sn^{4+} , the SnS_2 nanoparticles tend to nucleate and grow onto the GO substrate. For bare SnS_2 , when it is formed in the solution, it preferentially grows along the energetically stable (001) facet-terminated SnS_2 is relatively lower than (101) facet¹². However, after the addition of GO, the abundant oxygen-containing functional groups on the GO play a role in the production of inducing growth effect, which can promote the formation of the (101) surfaces of SnS_2 and lead to a smaller sizes of the nanoparticles¹³. Therefore, without addition of GO, both bare SnS_2 and $\text{Sn}_{0.9}\text{Co}_{0.1}\text{S}_x$ show flake-like structures (Supplementary Figs. 3 a-d and Supplementary Figs. 4 a-f), but the morphology of $\text{Sn}_{0.9}\text{Co}_{0.1}\text{S}_x$ evolved to smaller flakes with a

thickness around 2 nm as shown in Fig. 3c, d, which further confirmed the restricted growth of the (001) plane of SnS_2 due to the addition of Co. After measuring the (100) lattice spacing, it is found that the Co doping generated an expansion of the interlayer spacing in the SnS_2 crystal lattice, which is consistent with the XRD results.

The C1s XPS of $\text{Sn}_{0.9}\text{Co}_{0.1}\text{S}_x/\text{RGO}$ and SnS_2/RGO are shown in Fig. 4a, b. Generally, the carbon spectra can be deconvoluted into several peaks for carbon atoms in different functional groups: nonoxygenated carbon ($\text{C}=\text{C}$ at 284.6 eV and $\text{C}-\text{C}$ at 285.7 eV), carbon in $\text{C}-\text{S}$ bonds (286.5 eV), carbon in $\text{C}-\text{O}$ bonds (286.8 eV), carbonyl carbon ($\text{C}=\text{O}$, 288.0 eV) and carbon in $\text{O}-\text{C}=\text{C}$ (289.2 eV)¹⁴. It is evident from Fig. 4a, b that some O atoms in GO have been successfully substituted by S atoms, leading to S doping effect on the RGO. The presence of these $\text{C}-\text{S}$ bonds in the RGO also indicates that the S atoms exist inside the lattice and are covalently bonded to the RGO structure. Notably, this S doping effect as well as the small amount of oxygen-containing

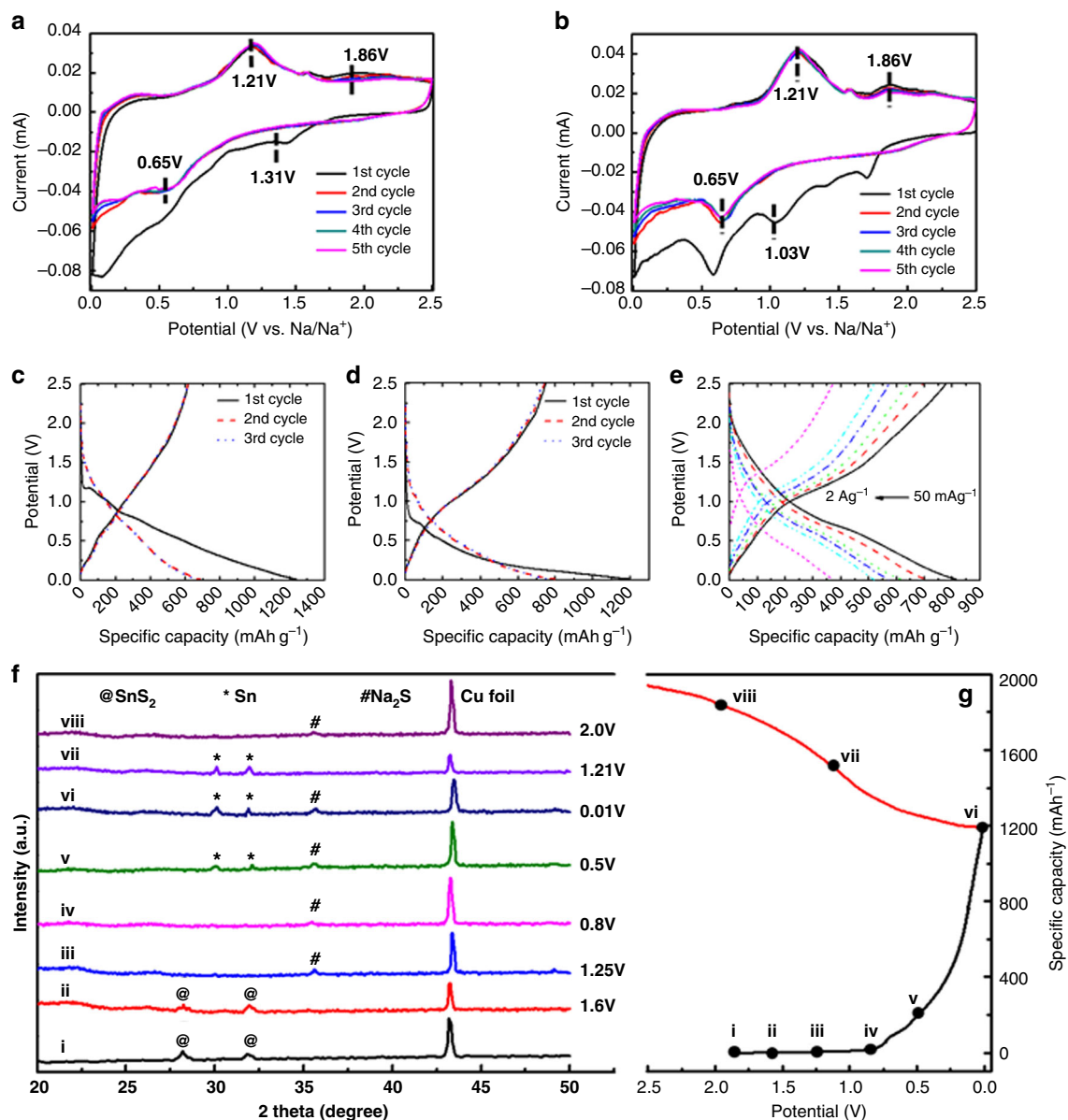


Fig. 5 Cycling performances of SnS_2/RGO before and after Co doping. Cyclic voltammograms of **a** SnS_2/RGO and **b** $\text{Sn}_{0.9}\text{Co}_{0.1}\text{S}_x/\text{RGO}$; First three charge/discharge profiles of the cells with **c** SnS_2/RGO and **d** $\text{Sn}_{0.9}\text{Co}_{0.1}\text{S}_x/\text{RGO}$ electrodes at a current density of 50 mA g^{-1} ; **e** charge/discharge profiles of the cell with $\text{Sn}_{0.9}\text{Co}_{0.1}\text{S}_x/\text{RGO}$ electrode under different current densities in the rate performance. **f** (i) Ex situ XRD patterns of the $\text{Sn}_{0.9}\text{Co}_{0.1}\text{S}_x/\text{RGO}$ electrode collected at various potential points, as indicated in the corresponding charge/discharge profiles. **(g)**: (i) Fresh electrode, (ii) after first discharge to 1.6 V, (iii) after first discharge to 1.25 V, (iv) after first discharge to 0.8 V, (v) after first discharge to 0.5 V, (vi) after first discharge to 0.01 V, (vii) after first charge to 1.21 V, and (viii) after first charge to 2.0 V. The at sign, asterisk, and hash represent characteristic XRD patterns of SnS_2 , Sn, and Na_2S , respectively. The discharge capacities of SnS_2/RGO and $\text{Sn}_{0.9}\text{Co}_{0.1}\text{S}_x/\text{RGO}$ in the first cycle were higher than the theoretical capacities of SnS_2 , which can be attributed to the formation of solid electrolyte interphase (SEI) and the reversible and irreversible insertion of the Na^+ in both RGO and SnS_2 . All the peaks in the CV curves for the 2nd and 3rd cycles overlapped, suggesting excellent reversibility of the $\text{Sn}_{0.9}\text{Co}_{0.1}\text{S}_x/\text{RGO}$ for Na storage

groups in the RGO can make the graphene more electron-rich, which is beneficial to the dispersion and anchoring of the $\text{Sn}_{0.9}\text{Co}_{0.1}\text{S}_x$ and SnS_2 nanoparticles and lead to a strong and intimate electronic coupling between the nanoparticles and the RGO^{8,10}. Figure 4c, d show that the S 2p spectra can be divided into two types of doublets. The peaks centered at 161.4 eV and 162.7 eV could be ascribed to the binding energies of S^{2-} in the SnS_2 , and the minor peaks located at 163.8 eV and 164.9 eV could be assigned to the formation of C–S bonds with lower valence states, as a result of the covalent bonding of S atoms to carbon atoms in a heterocyclic configuration^{9–11}. In the case of

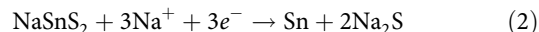
$\text{Sn}_{0.9}\text{Co}_{0.1}\text{S}_x/\text{RGO}$ composite, the Co peaks at 781.0 eV and 796.4 eV are detected in the XPS, as shown in Fig. 4e. The intensity of these two cobalt peaks are relatively weak because of the low content of Co in the $\text{Sn}_{0.9}\text{Co}_{0.1}\text{S}_x/\text{RGO}$. Two strong peaks located at about 486.6 and 495.1 eV in Fig. 4f corresponded to $\text{Sn } 3d_{3/2}$ and $\text{Sn } 3d_{5/2}$ of Sn^{4+} , respectively.

Electrochemical characterization. CV measurements were performed in the 0.01 to 2.5 V potential region at 0.05 mV s^{-1} to investigate the electrochemical reaction process. In the first scan

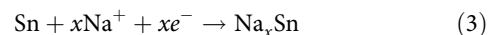
of SnS₂/RGO composite (Fig. 5a), the broad cathodic peak around 1.31 V could be assigned to Na intercalation of SnS₂ layers without phase decomposition and another cathodic peak at 0.58 V corresponded to a reduction reaction, which leads to the formation of metallic Sn and Na₂S. In the subsequent cycles, this peak shifted to 0.65 V and kept stable. In addition, as the cell was kept discharging to a lower potential (<0.65 V), another broad peak showed up, which could be attributed to the formation of irreversible solid electrolyte interphase (SEI) in the initial cycle. In the anodic process, several oxidation peaks located at 1.21 V and 1.86 V were detected. These oxidation peaks may be identified as the restitution of the SnS₂. In the case of the Sn_{0.9}Co_{0.1}S_x/RGO composite (Fig. 5b), all the cathodic and anodic peaks were observed at the same locations similar to those in SnS₂/RGO. Notably, the cathodic peak around 0.65 V in the first cycle and subsequent scans suggest a phase transformation reaction during the first cycle⁹. Exceptionally, compared with the CV curves of Sn_{0.9}Co_{0.1}S_x nanoparticles (Supplementary Fig. 5), the oxidation peaks at 0.25 V and 0.75 V were inconspicuous due to the imperfect crystallinity of SnS₂, which was induced by the Co doping¹⁵. It is worth noting that all the peaks in the CV curves for the 2nd and 3rd cycles overlapped, which indicates excellent reversibility of the Sn_{0.9}Co_{0.1}S_x/RGO for Na storage. The electrochemical performance of the SnS₂/RGO and Sn_{0.9}Co_{0.1}S_x/RGO as an SIB anode were evaluated in the voltage range of 0.01–2.5 V (vs Na⁺/Na) at a current density of 50 mA g^{−1}. The charge and discharge capacities for SnS₂/RGO and Sn_{0.9}Co_{0.1}S_x/RGO composites in the first cycle were determined to be 615.8, 749.0, and 1236.3, 1193.0 mAh g^{−1}, respectively, corresponding to a Coulombic efficiency of 49.8 and 62.8% (Fig. 5c, d). The discharge capacities of SnS₂/RGO and Sn_{0.9}Co_{0.1}S_x/RGO in the first cycle were higher than the theoretical capacities of SnS₂, owing to the formation of solid electrolyte interphase (SEI) and the reversible and irreversible insertion of the Na⁺ in both RGO and SnS₂. Note that Sn_{0.9}Co_{0.1}S_x/RGO exhibited higher Coulombic efficiency in the first cycle, this may be because the Co can facilitate reformation of Sn_{0.9}Co_{0.1}S_x and increase the reversibility of conversion reaction from Na₂S to SnS₂.

The possible mechanism of Sn_{0.9}Co_{0.1}S_x/RGO composite during the sodiation/desodiation reaction was further studied by ex situ XRD at different charge/discharge potentials in the first cycle (Fig. 5f). Similar to the Li⁺ intercalation process in the SnS₂ layers, the broad peak at 1.5–1.7 V in the first cathodic process (reduction) could be assigned to Na⁺ intercalation of the Sn_{0.9}Co_{0.1}S_x layers without phase decomposition (Fig. 5g). Under the voltage of around 1.6 V (stage ii), the electrode kept the same crystal structure as the pristine one, indicating that Na⁺ inserts into Sn_{0.9}Co_{0.1}S_x to form Na_xSn_{0.9}Co_{0.1}S_x by enlarging the layer spacing^{4,16,17}. Nevertheless, with the continuous Na⁺ intercalation, it is noticed that the electrode became amorphous after this discharging stage (stage iii), suggesting that the crystal structure of Na_xSn_{0.9}Co_{0.1}S_x broke down upon intercalating Na⁺ ions, because the layered structure cannot accommodate too many Na⁺ ions. Subsequently, as the electrode discharged to 1.25 V (ii), the electrode became amorphous, suggesting excess Na⁺ insertion into the layered structure and the crystal structure of Sn_{0.9}Co_{0.1}S_x broke down, leading to the disappearance of the Sn_{0.9}Co_{0.1}S_x peaks in the XRD pattern. As the potential continued to drop to 0.8 V, the electrode still showed amorphous characteristics, which attributes to a steep decrease in the charge/discharge curve¹⁸. It is worth mentioning that after the Na intercalation reaction, the conversion reaction occurs, resulting in the formation of SnS first⁴. However, in our study, the SnS peaks were not obvious in the XRD pattern (iv) and this could be ascribed to the relatively low SnS amount or the effect of Co doping, which may affect the conversion reaction from SnS₂

to SnS. Afterwards, the β-Sn phase in the following discharge process (0.5 V, v) via the following conversion reaction:



and an alloying reaction will occur simultaneously forming Na_xSn alloy^{4,18}



However, the peaks of Na_xSn were not visible in the XRD pattern, indicating an amorphous structure of the formed Na_xSn alloy. On the other hand, the peak of Na₂S was observed, which confirms the occurrence of the conversion reaction. As the cell was discharged to 0.01 V, the β-Sn peaks were still detectable and it reveals that the formation of a Na–Sn alloy occurred at lower voltage and the alloying reaction was not complete at 0.01 V. If the alloying reaction is complete, the β-Sn will fully transform into orthorhombic Na_{3.75}Sn after a two-phase reaction and it will experience a large lattice volume change (324% relative to SnS₂)¹⁸. Therefore, from the perspective of structural stability during cycling, properly increase the discharge potential can prevent the full sodiation of Sn_{0.9}Co_{0.1}S_x and large volume change, which is beneficial to the charge/discharge stability. During the charge process, the peaks corresponding to β-Sn gradually disappeared (from vii to viii) and this is indicative of the dealloying reaction of Na_xSn, leading to the formation of β-Sn and then its subsequent reaction with Na₂S, generating SnS or SnS₂. Particularly, the presence of the Na₂S peak upon charging to 2.0 V demonstrates that the conversion reaction in SnS₂ was partly reversible¹⁹, which may associate with the following two possible reasons: (1) the sluggish reaction kinetics; (2) the reformed Co structures have changed due to the various species of cobalt sulfides. Moreover, compared with the fresh electrode, the SnS₂ peaks were invisible after charging to 2.0 V, and this is probably due to the fact that the charged products (Sn_{0.9}Co_{0.1}S_x) were not well crystallized⁴.

As for the cycling stability, when cycled at a current density of 50 mA g^{−1}, the SnS₂/RGO and Sn_{0.9}Co_{0.1}S_x/RGO composites could maintain a high capacity of 511.5 and 636.2 mAh g^{−1} after 120 cycles, respectively, showing good capacity retention (Fig. 6a). It is well known that excellent rate capacity of the electrode plays a vital role for the applicability of the batteries. The rate performance of SnS₂, SnS₂/RGO, and Sn_{0.9}Co_{0.1}S_x/RGO composites were evaluated by increasing the current density gradually in steps from 0.05 to 2 A g^{−1} (Fig. 6b). For Sn_{0.9}Co_{0.1}S_x/RGO, the charge capacities at 0.05, 0.1, 0.2, 0.5, 1, and 2 A g^{−1} are determined to be 789.2, 693.2, 632.3, 569.1, 515.2, and 382.4 mAh g^{−1}, respectively. Compared with SnS₂/RGO and SnS₂, the rate performance of Co-doped anodes is superior to those of the undoped samples. As demonstrated in Fig. 5e, a modest charge/discharge plateau was still visible even at this high current, indicating a fast reaction kinetics and low polarization of Sn_{0.9}Co_{0.1}S_x/RGO composite. Remarkably, when the current was increased to 2 A g^{−1}, the Sn_{0.9}Co_{0.1}S_x/RGO composite still achieved a high capacity retention of 48.5% at 0.05 A g^{−1}. It should be noted that when the current was changed back to a low density, the capacity could be immediately recovered to the original value, demonstrating an ultra-fast charge/discharge process. For SnS₂/RGO, after the introduction of RGO, the rate performance was significantly increased and this phenomenon is associated with the synergic effect of SnS₂ with RGO^{9,20–22}. To illustrate the excellent performance of the rationally designed anode materials, the long-term cycling performance was tested under a current density of 1 A g^{−1}. As Fig. 6c shows, our results demonstrate that SnS₂/RGO and Sn_{0.9}Co_{0.1}S_x/RGO composites

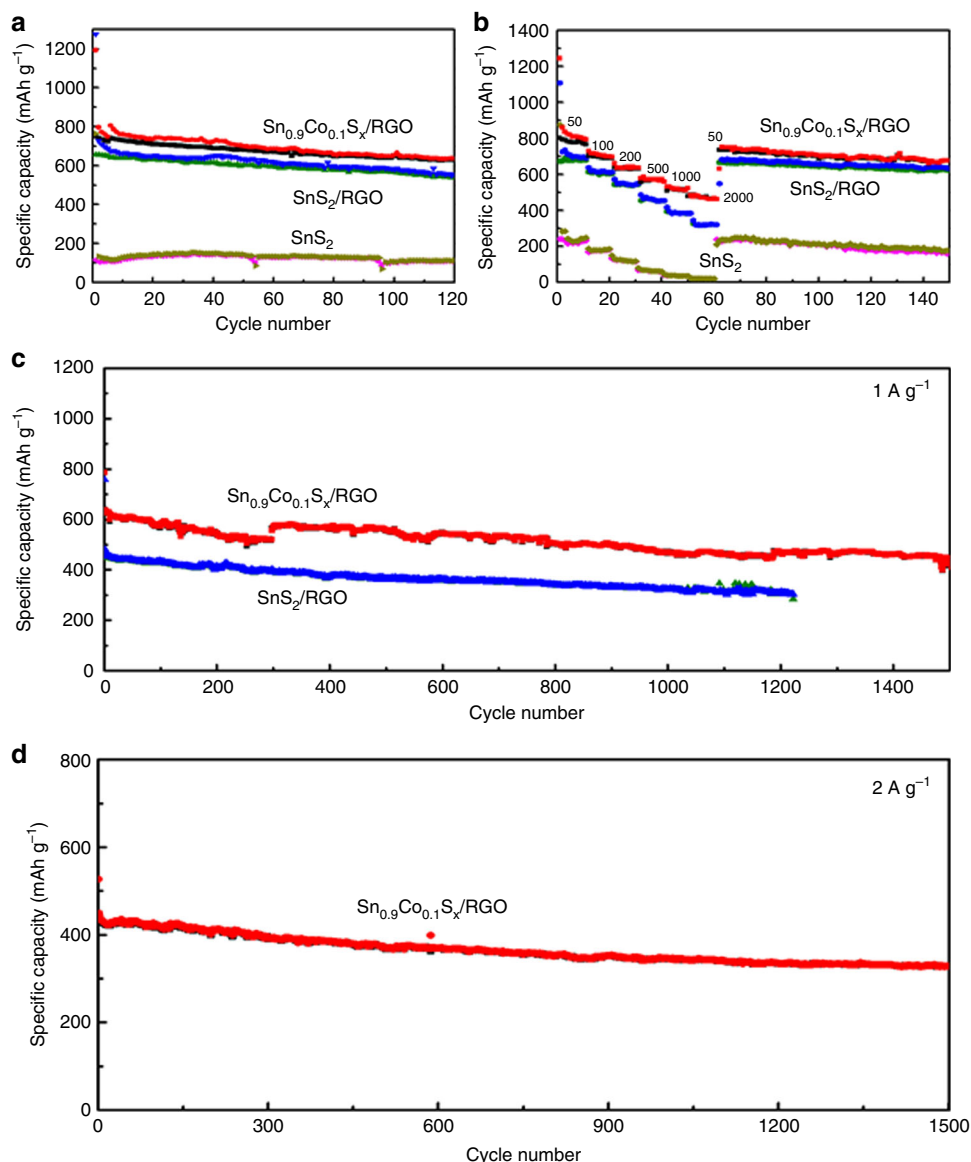


Fig. 6 Further cycling performances of SnS₂/RGO before and after Co doping. **a** Charging/discharging capacities plotted against the cycle number at a current density of 50 mA g⁻¹; **b** Rate performances of the cells with SnS₂ particles, SnS₂/RGO, and Sn_{0.9}Co_{0.1}S_x/RGO electrodes; **c** Long-term cycling performance of the cells with SnS₂/RGO and Sn_{0.9}Co_{0.1}S_x/RGO electrodes at a current density of 1 A g⁻¹; **d** Long-term cycling performance of the cells with Sn_{0.9}Co_{0.1}S_x/RGO electrodes at a current density of 2 A g⁻¹

still maintained a charge capacity of 322.5 and 452.2 mAh g⁻¹, respectively. Further increasing the current density to 2 A g⁻¹ (Fig. 6d), the Sn_{0.9}Co_{0.1}S_x/RGO still displayed a high capacity of 328.3 mAh g⁻¹ after 1500 cycles and these results proved excellent electrochemical durability of Sn_{0.9}Co_{0.1}S_x/RGO at a high current rate, which could be attributed to the following features. Firstly, the Co doping in the structure of SnS₂ limits the sizes and the number of layers of the nanosheets, also generates rich defects. In addition, the heteroatom doping could also gather pulverized SnS₂ during cycling and modify the strain and pressure from the volume change⁷. Therefore, the Co doping is beneficial to maintaining the integrated crystal structure during the charge/discharge process and improve the cycling stability. Secondly, homogeneous dispersed ultrafine Sn_{0.9}Co_{0.1}S_x nanoparticles on the flexible RGO could create a large electrode/electrolyte contact surface for shortening the Na⁺ diffusion and provide a large number of electrochemical active sites for Na⁺

storage. Finally, the S doping, which is confirmed by the XPS results, also makes the RGO more conductive, and it could greatly enhance the Na⁺ mobility rate.

To investigate the mechanism of the fast sodium storage kinetics of Sn_{0.9}Co_{0.1}S_x/RGO and SnS₂/RGO, CV tests were performed at various scan rates from 0.1 to 5 mV s⁻¹ (Fig. 7a). For Sn_{0.9}Co_{0.1}S_x/RGO, as the scan rate increased, the shape of the CV curves was preserved well, suggesting an extremely fast reaction and small polarization²³. The relationship between measured output current (*i*) and the sweep rate (*v*) could be described by the power law:

$$i = a v^b \quad (4)$$

where *i* is the measured current, *v* is the scan rate, both *a* and *b* are constants. When *b* is 0.5, the reaction shows a diffusion-controlled process and when *b* is 1, the surface-limited capacitive

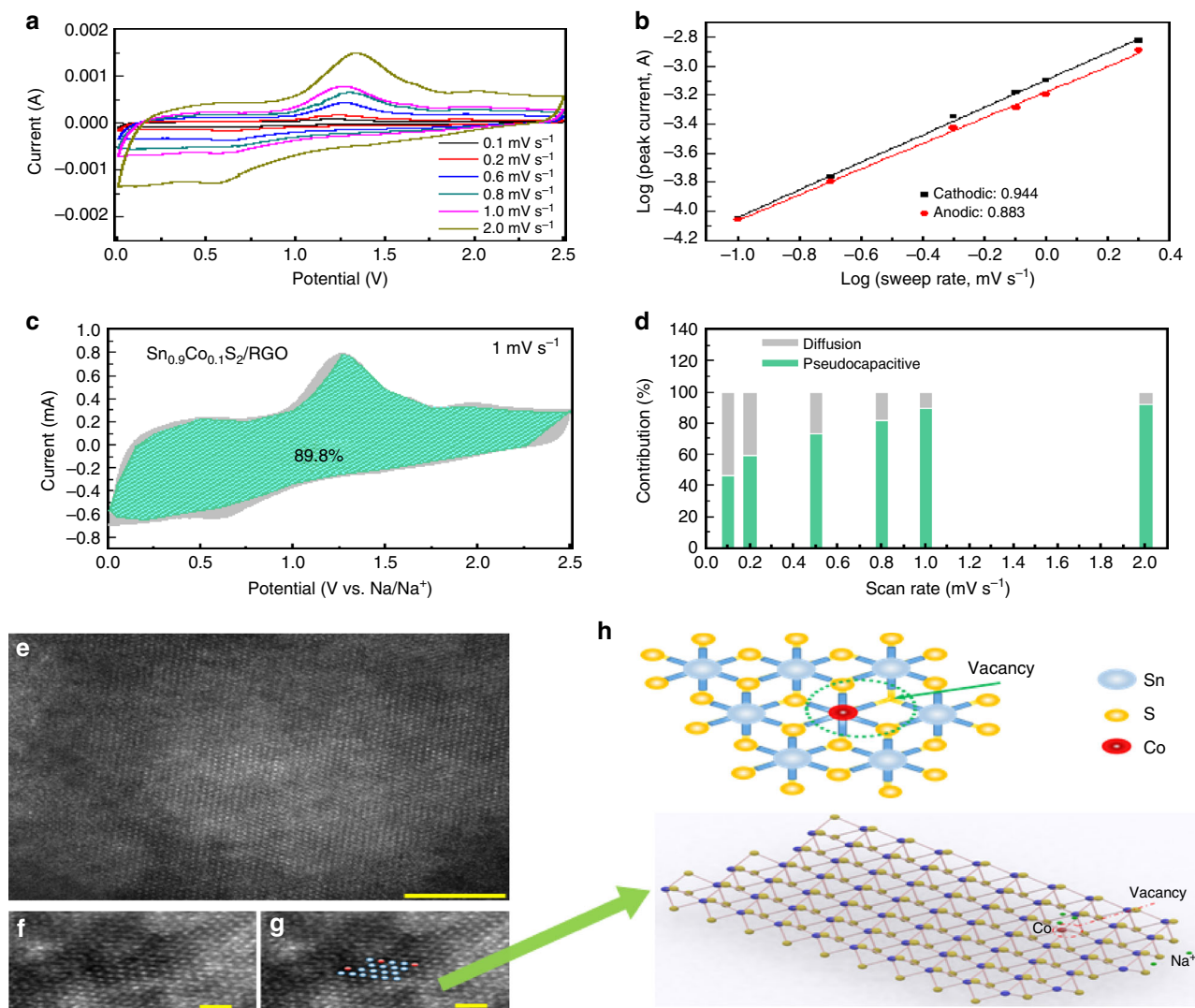


Fig. 7 Electrochemical performance and structural characterization of Co-doped SnS₂/RGO. **a** CV curves of Sn_{0.9}Co_{0.1}S_x/RGO at different scan rates; **b** current vs scan rate relationship for Sn_{0.9}Co_{0.1}S_x/RGO; **c** pseudocapacitance contribution at 1 mV s⁻¹; and **d** charge storage contributions at different scan rates. **e–g** HR-TEM images of Sn_{0.9}Co_{0.1}S_x/RGO. The scale bar represented 5 nm. **h** Schematic of Co atom location in the Sn_{0.9}Co_{0.1}S_x/RGO composite

behavior is dominant. The b value can be obtained from the slope of the $\log i$ versus $\log v$ plot (Fig. 7b). For both cathodic and anodic scans, the Sn_{0.9}Co_{0.1}S_x/RGO showed higher b values of 0.944 and 0.883, respectively, compared with SnS₂/RGO (Supplementary Fig. 6b), indicating a more favored capacitive kinetics. Moreover, the capacity contribution from capacitive and diffusion-controlled processes could be evaluated based on the following relationship:

$$i(V) = k_1 v + k_2 v^{1/2} \quad (5)$$

where $k_1 v$ is controlled by capacitive behavior and $k_2 v^{1/2}$ represents the diffusion-controlled contribution at certain voltage. As a result, at 1 mV s⁻¹, the pseudocapacitive contributes to 89.8% of the total capacity (Fig. 7c). From Fig. 7d, it is seen that as the sweep rates increased, the contribution from capacitive charge increased with a maximum value of ~96% at 2 mV s⁻¹, while the diffusion-limited intercalation contribution decreased. By the analysis, only 52.8% total capacity is identified

as the capacitive contribution for SnS₂/RGO at 1 mV s⁻¹ and this percentage of capacitive contribution is much lower than that of Sn_{0.9}Co_{0.1}S_x/RGO at different scan rates (Supplementary Fig. 6c,d). The large contribution from the pseudocapacitive reaction for Sn_{0.9}Co_{0.1}S_x/RGO can be ascribed to the structural merits as well as the Co doping effect. At first, the ultrafine nanoparticles and flexible RGO matrix would render a large contact surface with the electrolyte enabling shortened Na⁺ diffusion and enhanced kinetics. Second, the Co doping could cause some vacancies on the Sn_{0.9}Co_{0.1}S_x as shown in Fig. 7e–h and structurally, this would expose more Sn edges of SnS₂. The Sn edges and vacancies have lower adsorption energy, which are energetically favorable for hosting Na atoms²⁴. This kind of improvement on metal sulfide by doping another element has also been demonstrated by others^{25–27}. A proper combination of defects and topological disorders would generally create more energetically favorable structures and effectively facilitate the ion diffusions during the Na⁺ insertion and de-insertion processes. Therefore, Co doping created many feasible active sites for Na⁺ absorption with lower formation energy and

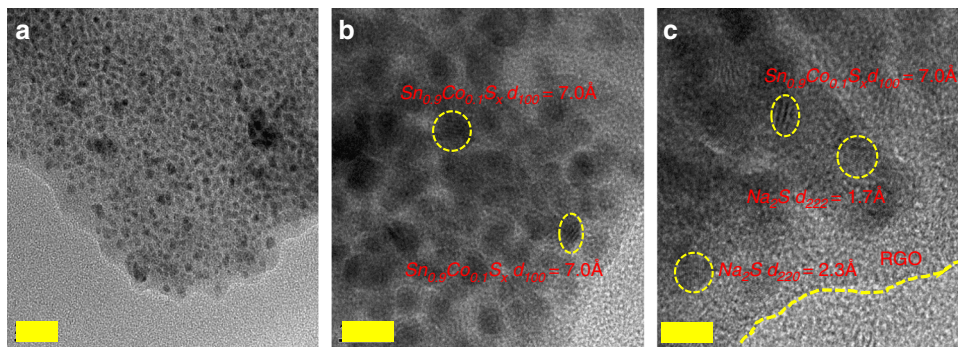


Fig. 8 Stability study. **a–c** TEM images of $\text{Sn}_{0.9}\text{Co}_{0.1}\text{S}_x/\text{RGO}$ after cycling at 1 A g^{-1} for 1500 cycles. The scale bars in **a–c** represent 20 nm, 10 nm, and 5 nm, respectively. The structural integrity of the RGO has been maintained. $\text{Sn}_{0.9}\text{Co}_{0.1}\text{S}_x/\text{RGO}$ loses the clear boundaries among nanoparticle structures and the d_{001} spacing of $\text{Sn}_{0.9}\text{Co}_{0.1}\text{S}_x/\text{RGO}$ is slightly enlarged to 7 Å because of the repeated Na alloying and dealloying

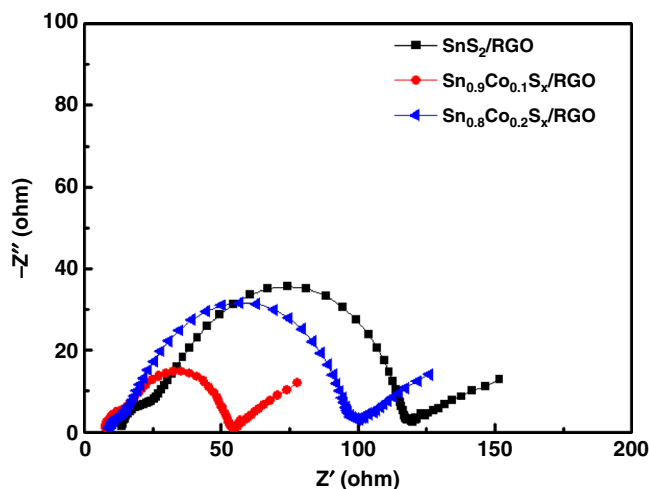


Fig. 9 Electrochemical properties. Electrochemical impedance spectra of the cells with SnS_2/RGO (black squares), $\text{Sn}_{0.9}\text{Co}_{0.1}\text{S}_x/\text{RGO}$ (red circles), $\text{Sn}_{0.8}\text{Co}_{0.2}\text{S}_x/\text{RGO}$ (blue triangles) electrodes. Co doping of SnS_2/RGO significantly improves the conductivity and diffusion of Na^+ . The diameter of semicircle for $\text{Sn}_{0.9}\text{Co}_{0.1}\text{S}_x/\text{RGO}$ is much smaller as compared to SnS_2/RGO in high-medium frequency region, suggesting lower contact and charge transfer resistance of $\text{Sn}_{0.9}\text{Co}_{0.1}\text{S}_x/\text{RGO}$ than those of SnS_2/RGO

contributed to the fast Na^+ storage. It is anticipated that these factors collaborate to induce the superior rate performance of $\text{Sn}_{0.9}\text{Co}_{0.1}\text{S}_x/\text{RGO}$.

After cycling at 1 A g^{-1} for 1500 cycles, the battery using $\text{Sn}_{0.9}\text{Co}_{0.1}\text{S}_x/\text{RGO}$ composite as the anode was disassembled and the electrode material was observed by TEM to evaluate its structural integrity. As is shown in Fig. 8a–c, the transparency of the RGO has been negatively influenced due to the contamination of the SEI layer, indicating an increased average thickness of the composite sheets. However, the structural integrity of the RGO was maintained and the $\text{Sn}_{0.9}\text{Co}_{0.1}\text{S}_x$ nanoparticles were still in intimate contact with the flexible RGO matrix. Especially, the $\text{Sn}_{0.9}\text{Co}_{0.1}\text{S}_x$ lost the clear boundaries among nanoparticle structures and the d_{001} spacing of $\text{Sn}_{0.9}\text{Co}_{0.1}\text{S}_x$ was slightly enlarged to 7 Å because of the repeated Na alloying and dealloying^{28–30}. Moreover, as the Fig. 8a–c demonstrate and some Na_2S dots were also detectable, which is in accord with the ex situ XRD results.

To further investigate the superior electrochemical properties of $\text{Sn}_{0.9}\text{Co}_{0.1}\text{S}_x/\text{RGO}$ by Co doping, electrochemical impedance spectroscopy (EIS) measurements were carried out. By comparing the Nyquist plots of $\text{Sn}_{0.9}\text{Co}_{0.1}\text{S}_x/\text{RGO}$ and SnS_2/RGO in Fig. 9, it confirmed that the Co doping to SnS_2/RGO could significantly improve the conductivity and diffusion of Na^+ . To be specific, their impedance spectra could be fitted to a semicircle in high frequency related to the SEI film impedance (R_s), a medium frequency semicircle corresponding to charge transfer resistance (R_{ct}) and an inclined line representing the Na^+ diffusion process, respectively. It is notable that the diameter of semicircle for $\text{Sn}_{0.9}\text{Co}_{0.1}\text{S}_x/\text{RGO}$ was much smaller as compared to SnS_2/RGO in high-medium frequency region, which revealed lower contact and charge transfer resistance of $\text{Sn}_{0.9}\text{Co}_{0.1}\text{S}_x/\text{RGO}$ than those of SnS_2/RGO . Additionally, the $\text{Sn}_{0.9}\text{Co}_{0.1}\text{S}_x/\text{RGO}$ exhibited a straighter inclined line in comparison to SnS_2/RGO , indicating the positive effect of Co doping in facilitating Na^+ diffusion.

Discussion

An anode material based on a few-layered SnS_2 with Co doping over an RGO matrix was synthesized in a few minutes by a microwave irradiation approach. The outstanding electrochemical performance of $\text{Sn}_{0.9}\text{Co}_{0.1}\text{S}_x/\text{RGO}$ may be attributed to a robust composite architecture that withstands the stress of cycling. First, the few-layered $\text{Sn}_{0.9}\text{Co}_{0.1}\text{S}_x$ nanocrystals over graphene sheets provide large contact area with the electrolyte and therefore fast pseudocapacitive Na^+ storage that enables better performance. Secondly, the synergistic interactions between the layered $\text{Sn}_{0.9}\text{Co}_{0.1}\text{S}_x$ and RGO contribute to the fast electron/ion transportation. The most important finding is that Co doping creates structural defects on the layered SnS_2 and allows for surface-dominated extrinsic pseudocapacitance instead of conventional solid-state diffusion, leading to superior rate performance. This work provides valuable insight into tuning the structure of layered transition metal dichalcogenides (TMDs) by heteroatom doping to promote high-rate performance of anode materials for high-performance SIBs.

Methods

Synthesis and characterization. Graphene oxide was first prepared by a modified Hummer's method³¹. For the synthesis of SnS_2/RGO , different amounts of $\text{SnCl}_4 \cdot 5\text{H}_2\text{O}$ and L-cysteine (1:4 mole ratio of Sn^{4+} to L-cysteine) were dissolved in a 50 mL GO ($\sim 1.5 \text{ mg mL}^{-1}$) solution under vigorous stirring. Then the solution was transferred into a round bottom flask and placed in a microwave oven. The solution was then irradiated for 10 min at 180°C . Subsequently, the obtained suspension was centrifuged, and washed three times each with deionized water and

absolute alcohol. The solid product was dried at 70 °C for 12 h in a vacuum oven. For the synthesis of Co-doped SnS₂/RGO, an appropriate amount of CoCl₂ (10%, depending on the molar ratio of Co to (Sn + Co)) was added to the SnCl₄ · 5H₂O, L-cysteine, and GO solution before microwave irradiation. Afterwards, the same microwave-assisted synthesis procedure as explained earlier would be carried out. The as-prepared products are denoted as Sn_{0.9}Co_{0.1}S₂/RGO. For comparison, pure SnS₂ and Co-doped SnS₂ samples and SnS₂/GO with different amounts of GO (15, 25, and 75 mL) were also prepared by the same synthetic route and denoted as SnS₂/15GO, SnS₂/25GO, SnS₂/75GO, respectively.

The crystal structure of the SnS₂/RGO and Co-doped SnS₂/RGO composites was studied by X-ray diffractometry (XRD, Rigaku SmartLab) with Cu Kα radiation between 2θ angles from 10° to 60°. Morphological features were examined by field-emission scanning electron microscopy (FE-SEM, FEI Verios 460 L), high-resolution transmission electron microscopy (HR-TEM, JEM-2010F), and aberration corrected STEM (FEI Titan 80–300), respectively. Raman spectra were obtained using a Renishaw-1000 Raman spectrometer with an excitation wavelength of 532 nm. The elemental chemical surface states were characterized by X-ray photoelectron spectroscopy (XPS) using a SPECS system with a PHOIBOS 150 analyzer.

Electrochemical measurements. SnS₂/RGO and Co-doped SnS₂/RGO composites were mixed with carbon black, alginate acid sodium salt binder, and deionized water to form a homogeneous slurry (weight ratios of 7:2:1). The slurry was then casted on a copper foil, followed by drying in a vacuum oven at 80 °C overnight to form the working electrodes. The half cells (CR2032) were assembled in an Ar-filled glovebox with a Na metal foil as the counter electrode, 200 μL of 1 M NaClO₄ in ethylene carbonate (EC)—diethyl carbonate (DEC)—fluoroethylene carbonate (FEC) (1:1:0.03 in volume) as the electrolyte and the glass fiber GF/D (Whatman) filter as the separator. Cyclic voltammetry (CV) measurements were carried out using a Gamry Reference 600 Potentiostat/Galvanostat/ZRA system in a potential window of 2.5–0.01 V. Galvanostatic charge–discharge tests were performed using a LAND CT2001A battery testing system in a voltage range of 0.01–2.5 V and the capacity values were calculated based on the total composite weight. For the ex situ XRD test, the cells were first discharged or charged to specific potential. Then the specific cells were disassembled in the glovebox and the electrodes were taken out from the coin cell and sealed in a thin transparent Kapton tapes to prevent them from contact with air and moisture.

Data availability

The authors can confirm that all relevant data are included in the article and/or its supplementary information files, or from the authors upon reasonable request.

Received: 25 June 2018 Revised: 22 October 2018 Accepted: 25 October 2018

Published online: 23 November 2018

References

- Chen, C. et al. In-situ formation of tin-antimony sulfide in nitrogen-sulfur Co-doped carbon nanofibers as high performance anode materials for sodium-ion batteries. *Carbon N. Y.* **120**, 380–391 (2017).
- Niu, F. et al. MoSe₂-covered N,P-doped carbon nanosheets as a long-life and high-rate anode material for sodium-ion batteries. *Adv. Funct. Mater.* **27**, 1–11 (2017).
- Zhang, Y. et al. Few-layered SnS₂ on few-layered reduced graphene oxide as Na-ion battery anode with ultralong cycle life and superior rate capability. *Adv. Funct. Mater.* **25**, 481–489 (2015).
- Sun, W. et al. Two-dimensional tin disulfide nanosheets for enhanced sodium storage. *ACS Nano* **9**, 11371–11381 (2015).
- Wang, Q., Huang, Y., Miao, J., Zhao, Y. & Wang, Y. Synthesis and electrochemical characterizations of Ce doped SnS₂ anode materials for rechargeable lithium ion batteries. *Electrochim. Acta* **93**, 120–130 (2013).
- Alqarni, A. S. & Yassin, O. A. Structural and optical properties of Fe-doped SnS₂ nanoflakes prepared by molten salt solid state reaction. *Mater. Sci. Semicond. Process.* **42**, 390–395 (2016).
- Chen, Q., Lu, F., Xia, Y., Wang, H. & Kuang, X. Interlayer expansion of few-layered Mo-doped SnS₂ nanosheets grown on carbon cloth with excellent lithium storage performance for lithium ion batteries. *J. Mater. Chem. A* **5**, 4075–4083 (2017).
- Liu, S. et al. Preferential c-axis orientation of Ultrathin SnS₂ nanoplates on graphene as high-performance anode for li-ion batteries. *ACS Appl. Mater. Interfaces* **5**, 1588–1595 (2013).
- Fan, L. et al. Promising dual-doped graphene aerogel/SnS₂ nanocrystal building high performance sodium ion batteries. *ACS Appl. Mater. Interfaces* **10**, 2637–2648 (2018).

- Wang, X. et al. Sulfur covalently bonded graphene with large capacity and high rate for high-performance sodium-ion batteries anodes. *Nano Energy* **15**, 746–754 (2015).
- Zhang, S., Yao, F., Yang, L., Zhang, F. & Xu, S. Sulfur-doped mesoporous carbon from surfactant-intercalated layered double hydroxide precursor as high-performance anode nanomaterials for both Li-ion and Na-ion batteries. *Carbon N. Y.* **93**, 143–150 (2015).
- Zhang, Z. et al. (101) Plane-oriented SnS₂ nanoplates with carbon coating: a high-rate and cycle-stable anode material for lithium ion batteries. *ACS Appl. Mater. Interfaces* **9**, 35880–35887 (2017).
- Xiao, J. et al. Exfoliated MoS₂ nanocomposite as an anode material for lithium ion batteries. *Chem. Mater.* **22**, 4522–4524 (2010).
- Poh, H. L., Šimek, P., Sofer, Z. & Pumera, M. Sulfur-doped graphene via thermal exfoliation of graphite oxide in H₂S, SO₂, or CS₂ gas. *ACS Nano* **7**, 5262–5272 (2013).
- Zhou, P. et al. SnS₂ anowall arrays toward high-performance sodium storage. *ACS Appl. Mater. Interfaces* **9**, 6979–6987 (2017).
- Qu, B. et al. Layered SnS₂-reduced graphene oxide composite - a high-capacity, high-rate, and long-cycle life sodium-ion battery anode material. *Adv. Mater.* **26**, 3854–3859 (2014).
- Xie, X. et al. SnS₂ nanoplatelet/graphene nanocomposites as high-capacity anode materials for sodium-ion batteries. *Chem. - Asian J.* **9**, 1611–1617 (2014).
- Zhou, T., Pang, W., Zhang, C., Yang, J. & Chen, Z. Enhanced sodium-ion battery performance by structural phase transition from two-dimensional hexagonal-SnS₂ to orthorhombic-SnS. *ACS Nano* **8**, 8323–8333 (2014).
- Jiang, Y., Wei, M., Feng, J., Ma, Y. & Xiong, S. Enhancing the cycling stability of Na-ion batteries by bonding SnS₂ ultrafine nanocrystals on amino-functionalized graphene hybrid nanosheets. *Energy Environ. Sci.* **9**, 1430–1438 (2016).
- Cui, C. et al. Growth of NiCo₂O₄@MnMoO₄ Nanocolumn arrays with superior pseudocapacitor properties. *ACS Appl. Mater. Interfaces* **8**, 8568–8575 (2016).
- Li, S. et al. Surface capacitive contributions: towards high rate anode materials for sodium ion batteries. *Nano Energy* **12**, 224–230 (2015).
- Chao, D. et al. Array of nanosheets render ultrafast and high-capacity Na-ion storage by tunable pseudocapacitance. *Nat. Commun.* **7**, 12122 (2016).
- Ma, C. et al. Investigating the energy storage mechanism of SnS₂-rGO composite anode for advanced Na-Ion batteries. *Chem. Mater.* **27**, 5633–5640 (2015).
- Cui, J. et al. Revealing pseudocapacitive mechanisms of metal dichalcogenide SnS₂/graphene-CNT aerogels for high-energy Na hybrid capacitors. *Adv. Energy Mater.* **8**, 1702488 (2017).
- Mukherjee, S., Banwait, A., Grixti, S., Karateka, N. & Singh, C. V. Adsorption and diffusion of lithium and sodium on defective rhenium disulfide: A first principles study. *ACS Appl. Mater. Interfaces* **10**, 5373–5384 (2018).
- Wang, W. et al. First-principles investigations of vanadium disulfide for lithium and sodium ion battery applications. *RSC Adv.* **6**, 54874–54878 (2016).
- Liang, P. et al. Is borophene a suitable anode material for sodium ion battery? *J. Alloy. Comp.* **704**, 152–159 (2017).
- Guo, J., Jiang, B., Zhang, X. & Liu, H. Monodisperse SnO₂ anchored reduced graphene oxide nanocomposites as negative electrode with high rate capability and long cyclability for lithium-ion batteries. *J. Power Sources* **262**, 15–22 (2014).
- Zhou, X. et al. Tin dioxide@carbon core-shell nanoarchitectures anchored on wrinkled graphene for ultrafast and stable lithium storage. *ACS Appl. Mater. Interfaces* **6**, 7434–7443 (2014).
- Li, N., Song, H., Cui, H. & Wang, C. SnO₂ nanoparticles anchored on vertically aligned graphene with a high rate, high capacity, and long life for lithium storage. *Electrochim. Acta* **130**, 670–678 (2014).
- Marciano, D. C. et al. Improved synthesis of graphene oxide. *ACS Nano* **4**, 4806–4814 (2010).

Acknowledgements

The authors are grateful for the financial support of this project by the U.S. National Science Foundation (Award # 1523617 and Award # 1831133). This work was performed in part at the Analytical Instrumentation Facilities (AIF) at NC State University, which is supported by the state of North Carolina and the National Science Foundation (Award ECCS-1542015). A.I.F. is a member of RTNN, a site in the National Nanotechnology Coordinated Infrastructure (NNCI).

Author contributions

C.C., H.J., and F.Y. conceived the experiment. C.C., O.O. G.L., and H.J. performed the experiments. Y.T. and X.Z. were involved in scientific discussion. All authors participated

in data analysis and contributed to the writing of the manuscript. F.Y. directed the research.

Additional information

Supplementary information accompanies this paper at <https://doi.org/10.1038/s42004-018-0086-z>.

Competing interests: The authors declare no competing interests.

Reprints and permission information is available online at <http://npg.nature.com/reprintsandpermissions/>

Publisher's note: Springer Nature remains neutral with regard to jurisdictional claims in published maps and institutional affiliations.



Open Access This article is licensed under a Creative Commons Attribution 4.0 International License, which permits use, sharing, adaptation, distribution and reproduction in any medium or format, as long as you give appropriate credit to the original author(s) and the source, provide a link to the Creative Commons license, and indicate if changes were made. The images or other third party material in this article are included in the article's Creative Commons license, unless indicated otherwise in a credit line to the material. If material is not included in the article's Creative Commons license and your intended use is not permitted by statutory regulation or exceeds the permitted use, you will need to obtain permission directly from the copyright holder. To view a copy of this license, visit <http://creativecommons.org/licenses/by/4.0/>.

© The Author(s) 2018